Polymer Chemistry

ROYAL SOCIETY OF CHEMISTRY

PAPER

View Article Online
View Journal | View Issue

Cite this: *Polym. Chem.*, 2025, **16**, 2421

Corona-shaped two-dimensional polyaramid derivatives for poly(ethylene oxide)-based all-solid-state lithium batteries†

Feifan Zheng,[a] Liping Jiang,[a] Xiaoli Gong,[a] Zhengqiao Yin,[a] Fei Wang [b] and Yuwen Zeng *[a]

Solid polymer electrolytes (SPEs), especially those based on poly(ethylene oxide) (PEO), have garnered significant attention in the field of all-solid-state lithium batteries due to their high processability and low cost, advantages that are typically hard to achieve with their inorganic counterparts. However, their poor ionic conductivities have retarded their further application in all-solid-state lithium batteries. Herein, we report a series of corona-shaped two-dimensional polyaramid (2DPA) derivatives that improve the overall performance of PEO-based SPEs, including ionic conductivity, ion transference number, and electrochemical stability. We demonstrate that the unique corona topology, consisting of a rigid two-dimensional polyaramid core and flexible poly(ethylene glycol) (PEG) chains grafted at its periphery, effectively inhibits the crystallization of the PEO matrix through chain entanglement, thus enhancing ionic conductivity. Furthermore, the 2D polyaramid core provides enriched Lewis acidic binding sites for counter anions, suppressing the anion motion and resulting in selective lithium-ion transport. Therefore, a blend of 30% 2DPA-PEGs and PEO exhibits an enhanced room temperature ionic conductivity up to 4.39×10^{-5} S cm^{-1} (an order of magnitude higher than that of the original SPE), an elevated lithium-ion transference number of 0.78, and a high oxidation voltage of 4.7 V (*vs.* Li/Li^{+}). Meanwhile, the assembled all-solid-state batteries exhibit improved cycling performance and higher stability. Such a heterostructural polymer design strategy showcases the promising potential of novel 2D polymer derivatives for ion transport optimization in SPEs.

Received 14th January 2025,
Accepted 16th April 2025

DOI: 10.1039/d5py00046g

rsc.li/polymers

Introduction

The rising demand for electric vehicles and portable devices, which calls for higher energy and power density, has made lithium metal batteries a primary focus for next-generation energy storage.[1–3] Despite its exceptionally high theoretical specific capacity of 3860 mA h g^{-1}, the lithium metal anode suffers from significant safety challenges, including unsuppressed dendrite growth and an unstable solid electrolyte interphase when paired with traditional liquid electrolytes.[4,5] Solid-state electrolytes, known for their intrinsic mechanical robustness and chemical stability, are emerging as a viable alternative to liquid electrolytes, offering a potential solution to the challenges associated with lithium metal anodes.[6,7]

Solid-state electrolytes, which have been extensively investigated for decades, are categorized into two main types: solid polymer electrolytes (SPEs) and inorganic solid electrolytes (ISEs). SPEs, notably poly(ethylene oxide) (PEO)-based ones, are typically more cost-effective, processable, and flexible than ISEs.[6,8,9] However, their inferior room-temperature ionic conductivity at 10^{-8} to 10^{-6} S cm^{-1} has hindered their broader application.[10–12] In addition, the low lithium transference number and oxidation voltage of PEO-based SPEs further deteriorate their cycling performance.[13–17] Lithium-ion transport in PEO-based SPEs, which is highly affected by the chain segment mobility, almost exclusively occurs in the amorphous region through ion hopping among coordination sites within polymer chains.[18,19] To reduce the crystallinity of SPEs and further enhance their ionic conductivity, researchers have focused on incorporating functional fillers into the PEO matrix to inhibit chain crystallization.[20–24] However, such a strategy necessitates a high specific surface area coupled with strong interactions between the fillers and polymer chains,[25–27] a combination that is often difficult to attain in inorganic systems. This difficulty leads to the undesired aggregation of fillers within electrolyte composites, further impeding ionic conductivity, processability, and mechanical properties.[28–30]

[a]*State Key Laboratory of Molecular Engineering of Polymers, Department of Macromolecular Science, Fudan University, Shanghai, 200438, China. E-mail: zengy@fudan.edu.cn*
[b]*Department of Materials Science, Shanghai Key Laboratory of Molecular Catalysis and Innovative Materials, Fudan University, Shanghai 200433, China*
† Electronic supplementary information (ESI) available. See DOI: https://doi.org/10.1039/d5py00046g

The emerging two-dimensional polyaramid (2DPA),[31] synthesized *via* an irreversible 2D polymerization of 1,3,5-benzenetricarboxylic chloride (TMC) and melamine (MA), combines the high specific surface area and chemical stability of conventional 2D materials with the ease of modification characteristic of organic systems, making it a promising 2D molecular platform for the development of 2D functional materials. We envision that after peripheral functionalization of individual 2DPA platelets with PEG chains, the resulting corona-shaped polymers, termed 2DPA-PEG, can serve as molecular fillers, featuring a rigid discotic core with dense and flexible PEG chains. Here, the introduction of PEG chains, selected for their PEO-homogenic nature, is performed for intrinsic compatibility with the electrolyte matrix, therefore preventing the undesired filler aggregation. On the one hand, PEG chains are effectively embedded and thus entangled within the PEO chains, while on the other hand, the irregular shape of 2DPA-PEG and the insufficient chain length of PEG impede the crystallization process, preserving the amorphous nature of PEO. Meanwhile, the highly exposed 2DPA core possesses enriched Lewis acidic bonding sites (–NH– in amides), which could potentially interact with counter anions and suppress their motion to obtain a higher lithium-ion transference number. Furthermore, due to the electron-deficient nature of the triazine motif, the electrochemical stability of 2DPA-PEG would be improved compared to that of PEO.

In this work, we report a series of PEG-grafted 2DPA derivatives characterized by a corona-like topological structure. These derivatives were synthesized *via* a one-pot approach that included an irreversible 2D polymerization,[31] followed by the post-modification of the resulting 2D platelets' periphery with short PEG chains. The PEG-grafted 2DPA derivatives are miscible with the PEO matrix due to the entanglement of PEG and PEO chains, an interaction that effectively prevents PEO crystallization and, as a result, enhances their ion transport behaviours. We also found that this 2DPA-PEG/PEO blend (denoted as 2DPA-SE) exhibits ionic conductivities of 4.39×10^{-5} S cm^{-1} at room temperature and 2.17×10^{-4} S cm^{-1} at 50 °C, a high lithium-ion transference number (0.78) and a high oxidation voltage (4.7 V, *vs.* Li/Li^{+}). The assembled lithium symmetric cell stably cycled for over 1400 h without short-circuits at 0.05 mA h cm^{-2} and the battery of Li|LiFePO$_4$ showed a discharge capacity of 149.2 mA h g^{-1} with a coulombic efficiency of 99.6% after 50 cycles at 0.2 C.

Results and discussion

The precursor of 2DPA-PEG, which is a 2D polyaramid core, is constructed through an irreversible polymerization of TMC and MA in solution under ambient conditions.[31] Following this transformation, the resulting 2DPA platelets with abundant residual acyl chlorides (–COCl) at their edges are quenched with HO-PEG-OCH$_3$ of varying molecular weights (350, 550, 750, and 1000 g mol^{-1}), yielding the desired heterostructural polymers (Fig. 1a). The chemical structure of 2DPA-PEG was characterized by Fourier transform infrared (FTIR) spectroscopy (Fig. S1†), in which characteristic peaks of amide (1600–1700 cm^{-1}),[31,32] ester (~1720 cm^{-1}),[33,34] and ether (~1110 cm^{-1}) indicate the successful mounting of PEG

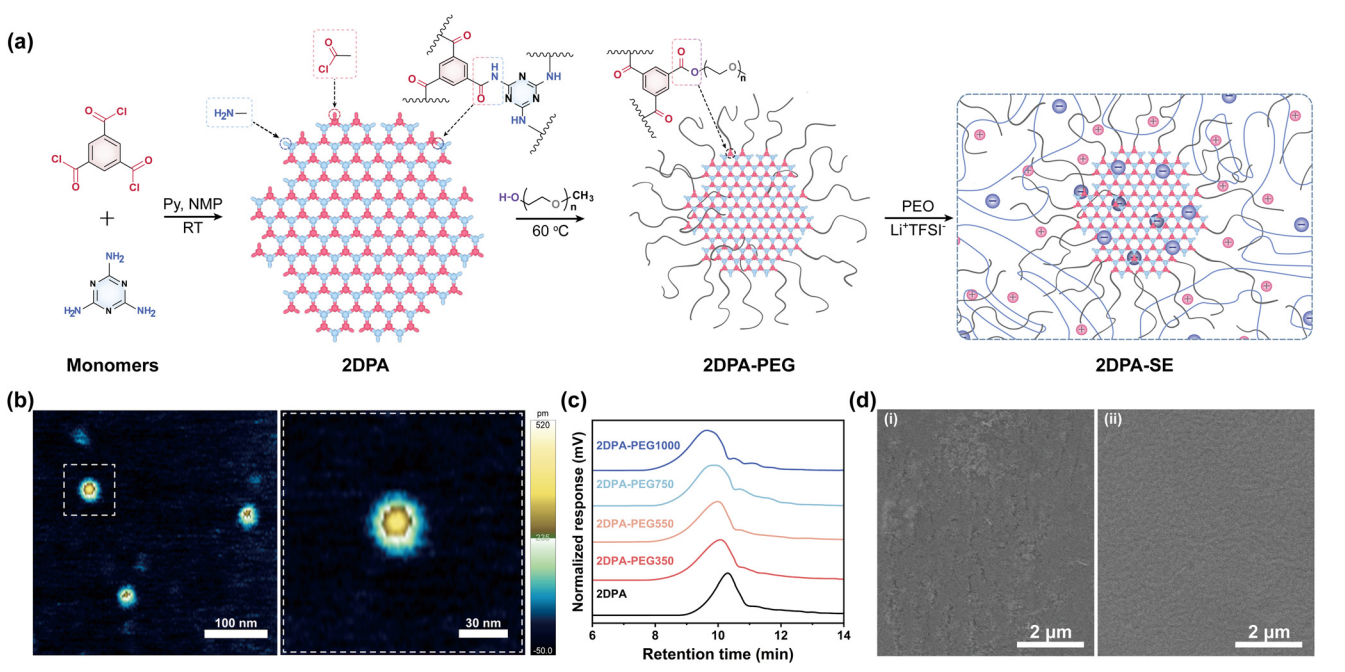

Fig. 1 (a) The synthesis of 2DPA-PEG and the fabrication of 2DPA-SE. (b) The high-resolution atomic force microscopy (AFM) image of 2DPA-PEG1000 and its zoomed-in version. (c) The gel permeation chromatography (GPC) curves of 2DPA-PEGs. (d) The scanning electron microscopy (SEM) images of the electrolyte surfaces of (i) PEO/LiTFSI and (ii) 30-2DPA-SE.

chains onto 2DPA cores. Further ^{1}H NMR analysis (Fig. S2 and S3†) reveals high conversion rates (>90%) of –COCl to –COO-PEG-OCH$_3$, according to the ratio of characteristic peak areas around 4.5 ppm (–COOCH$_2$–, a product of –COCl with HO-PEG-OCH$_3$) and 13–14 ppm (–COOH, a byproduct of –COCl with moisture). The unique corona shape of the individual 2DPA-PEG molecule is evidenced by the images in Fig. 1b and S4,† where a flat core of 2DPA is surrounded by an outer circle of PEG chains. To gain a better understanding of the grafting process, gel permeation chromatography (GPC) was employed to trace the molecular weight change (Fig. 1c and S5†). Upon the quenching of PEG, the retention time of 2DPA (10.31 min) is reduced, while the higher homologues such as 2DPA-PEG1000 possess a shorter retention time (9.64 min) than that of 2DPA-PEG350 (10.07 min). In addition, no crystallization or orientation is observed in the X-ray diffraction (XRD) spectra of 2DPA-PEGs (Fig. S6†).

After dissolving 2DPA-PEGs in *N*,*N*-dimethylformamide and mixing with PEO/lithium bis(trifluoromethanesulphonyl) imide (LiTFSI), homogeneous solutions are formed (Fig. S7†). Removal of the solvent under reduced pressure and elevated temperature leads to thin films without any phase separation or inhomogeneity, suggesting a uniform distribution of 2DPA-PEGs within the PEO matrix (Fig. 1d and S8†). Furthermore, the surface of the 2DPA-PEG/PEO/LiTFSI blend is noticeably smoother with fewer cracks compared to the PEO/LiTFSI blend. SPE films with different compositions and varying PEG chain lengths were then assembled with stainless steel to measure their ionic conductivities. In Fig. 2a, the SPE containing 30% 2DPA-PEG750 (denoted as 30-2DPA-SE) exhibits the highest room-temperature ionic conductivity of 4.39×10^{-5} S cm^{-1}, which is an order of magnitude higher compared to that of the original PEO electrolyte. Other SPEs containing 2DPA-PEGs exhibit inferior ionic conductivities compared to the 2DPA-PEG750 blend, suggesting that a molecular weight of 750 g mol^{-1} represents the optimal PEG chain length in this topological structure for facilitating ion transport. However, when a higher fraction of 2DPA-PEG750 (40%) is incorporated, the ionic conductivity decreases, a phenomenon also observed with other 2DPA-PEG derivatives. This decline can be attributed to the reduced fraction of flexible PEO chains, which are essential for ion hopping within the electrolyte. Furthermore, 2DPA-PEG/LiTFSI alone exhibits low ionic conductivity (Fig. S9†), and this conductivity further decreases as the length of the flexible PEG chain reduces. This indicates that the presence of the PEO matrix is crucial for establishing continuous ion transport pathways in the SPE design.

A decrease in activation energy (E_a) for ion transport from 1.087 eV to 0.389 eV is observed when 30% 2DPA-PEG750 is blended (Fig. 2b), supporting our hypothesis on the heterostructural molecular filler. Additionally, the transition of E_a at 55 °C in the original PEO/LiTFSI, which represents the melting of PEO crystals, is consistent with our differential scanning calorimetry (DSC) observations presented in Fig. 3b. In Fig. 2c,

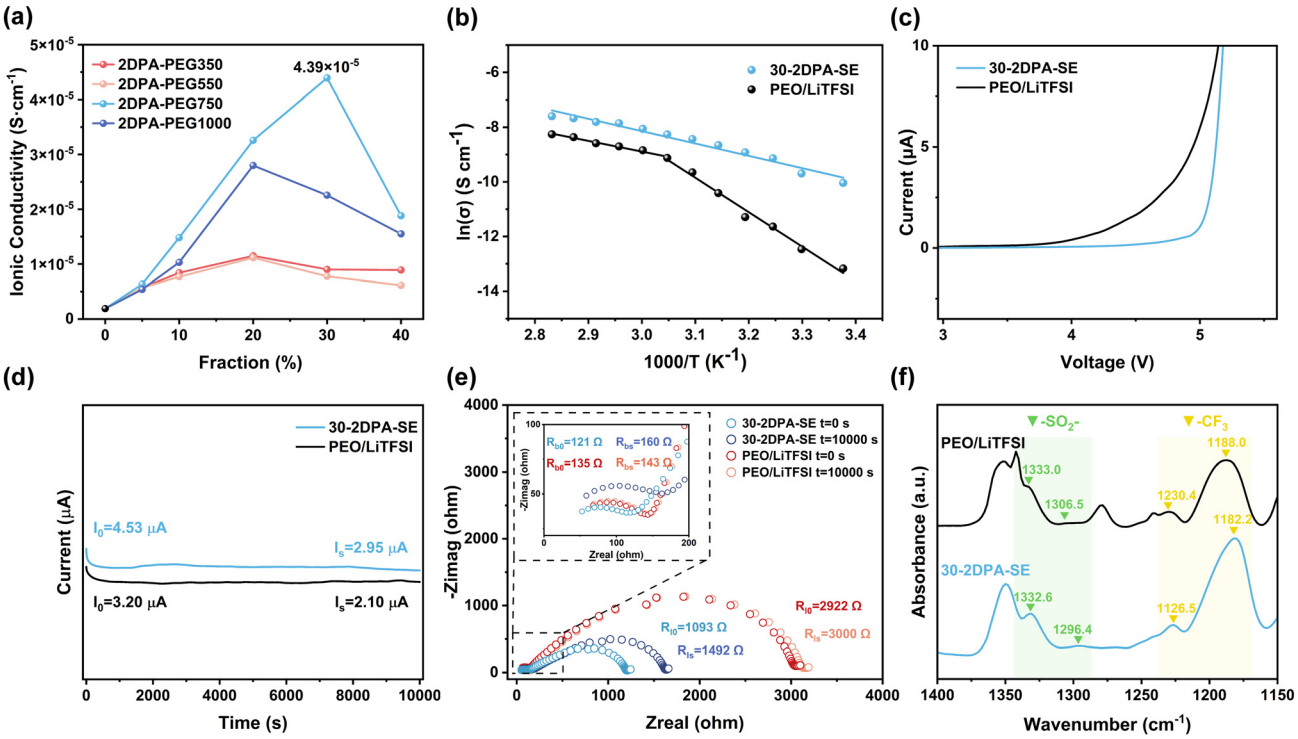

Fig. 2 (a) The ionic conductivities of PEO/LiTFSI blended with different fractions of 2DPA-PEGs at room temperature. (b) The ionic conductivities of SPEs at various temperatures. (c) The linear sweep voltammetry curves of SPEs at 0.5 mV s^{-1}. (d) The chronoamperometry curves over 10 000 s and (e) their corresponding electrochemical impedance spectra of SPEs. (f) The FTIR spectra and characteristic peaks of SPEs.

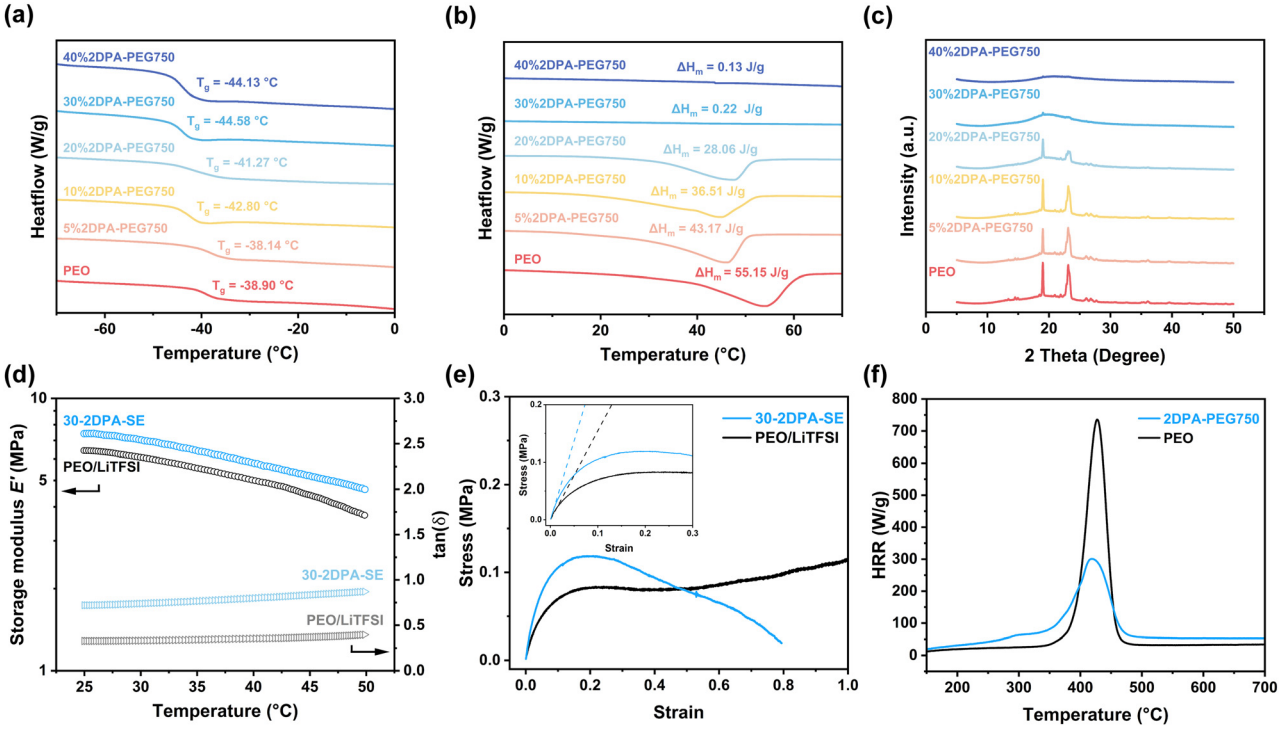

Fig. 3 (a) The differential scanning calorimetry (DSC) curves and glass transition temperatures of SPEs. (b) The DSC curves and melting enthalpies of SPEs. (c) The X-ray diffraction (XRD) spectra of SPEs. (d) The dynamic mechanical analysis (DMA) curves of SPEs from 25 to 50 °C. (e) The stress–strain curves of SPEs, from a strain of 0 to 1.0 (the full curve is shown in Fig. S12†). (f) The microscale combustion calorimetry (MCC) curves of SPEs.

the current plateau of the 2DPA-PEG750 blend is extended due to the good oxidation stability of triazine groups in the 2DPA core. Furthermore, 30-2DPA-SE exhibits stable performance at step voltage plateaus from 4.3 to 4.7 V at 50 °C (Fig. S10†), whereas the oxidation of the PEO/LiTFSI system starts below 4 V. This broader electrochemical window would enable more stable cycling performance for Li|LFP batteries using 30-2DPA-SE.

The lithium-ion transference number was calculated using the following equation: $t_{Li^+} = I_s R_{bs}(\Delta V - I_0 R_{l0})/I_0 R_{b0}(\Delta V - I_s R_{ls})$,[35] where ΔV is the applied potential (10 mV), R_b and R_l are the bulk and passivation layer resistances, and I is the current (the subscripts 0 and s refer to the initial and steady state, respectively). As shown in Fig. 2d and e, chronoamperometry tests and the corresponding electrochemical impedance measurements reveal a significant improvement in the lithium-ion transference number, increasing from 0.12 to 0.78 after the addition of 30% 2DPA-PEG750. This high transference number is expected to enhance cycling performance by reducing polarization.[36,37] The enhancement in lithium-ion transference number can be attributed to the Lewis acid–base interaction between the amide groups on the 2DPA cores and the $TFSI^-$ anions within the electrolyte. This interaction debilitates the movement of $TFSI^-$, resulting in a higher portion of Li^+ movement in ionic conduction.[10,29] Indeed, in the FTIR spectra of the electrolytes (Fig. 2f), the characteristic peaks of $TFSI^-$ ($-SO_2-$ and $-CF_3$) at 1333.0 cm^{-1}, 1306.5 cm^{-1}, 1230.4 cm^{-1}, and 1187.0 cm^{-1} red-shift to 1332.6 cm^{-1}, 1296.4 cm^{-1}, 1226.5 cm^{-1}, and 1182.2 cm^{-1}, respectively.[38]

As expected, the entanglements between PEG chains from 2DPA-PEGs and PEO chains interrupt the chain crystallization and increase the fraction of the amorphous region in the electrolyte. In Fig. 3a, the glass transition temperature (T_g) of SPEs, an indicator of chain segment mobility, overall decreases as the ratio of 2DPA-PEG750 increases. The lowest T_g is observed at a 30% 2DPA-PEG750 content, which matches well with our ionic conductivity results. More importantly, the enthalpy of melting (ΔH_m) of PEO blends diminishes with increasing content of 2DPA-PEG750, reaching almost zero at 30% of 2DPA-PEG750 (Fig. 3b). Other 2DPA-PEGs exhibit similar characteristics, as shown in Fig. S11,† in which polymers with longer PEG chain lengths show better performance in reducing crystallization. The crystallinity of the electrolytes was also evaluated using XRD (Fig. 3c), in which the characteristic crystalline peaks of PEO at 19.0° and 23.1° are effectively suppressed at 30% and 40% 2DPA-PEG750 contents, aligning with the same trend observed in ΔH_m. Therefore, all the results mentioned above confirm that the addition of 2DPA-PEGs reduces the proportion of crystalline regions within PEO.

Given the highest ionic conductivity and an almost zero proportion of crystalline regions, 30% 2DPA-PEG750 was selected for the subsequent study of SPEs. In Fig. 3d, 30-2DPA-SE exhibits enhanced mechanical properties in dynamic mechanical analysis (DMA), characterized by a higher storage

modulus (E') and tan(δ) compared to the original PEO solid electrolyte over the temperature range from 25 to 50 °C. The enhanced stiffness, resulting from the rigid 2D cores as well as the chain entanglements, is beneficial for suppressing dendrite growth. Meanwhile, the higher tan(δ) in 30-2DPA-SE is associated with better chain segmental mobility,[39,40] which in turn leads to enhanced ionic conductivity. The higher loss modulus (E'', $E'' = E' \times \tan(\delta)$) of 30-2DPA-SE also indicates a better capability for energy dissipation. The tensile test of 30-2DPA-SE yields an elastic modulus of 2.7 MPa and an acceptable elongation at break of 80% (Fig. 3e). This modulus is substantially higher than that of its PEO counterpart, which has a modulus of 1.5 MPa. In addition, 30-2DPA-SE exhibits good thermal stability, as evidenced by thermogravimetric analysis (TGA); no significant weight loss (5%) is observed until 322 °C (Fig. S13†). In the microscale combustion calorimetry (MCC) test (Fig. 3f and S14†), 2DPA-PEG750 presents a peak heat release rate (HRR) of 300.8 W g^{-1}, which is less than half of PEO's 735.6 W g^{-1}. This indicates a superior flame retardancy, which is due to the triazine groups in the 2DPA cores that decompose to form noncombustible gases and induce the formation of a char layer on the surface, thereby retarding further combustion.[41–43]

Lithium symmetric cells were assembled with 30-2DPA-SE and PEO/LiTFSI to compare their stability with lithium metal and their ability to suppress dendrite growth. As depicted in Fig. 4a, the symmetric cells were charged/discharged for 1 hour at a current density of 0.05 mA cm^{-2}. The cell with 30-2DPA-SE exhibits a significantly lower initial overpotential of 24 mV than that of PEO/LiTFSI, which slowly rises to 43 mV after 100 h. The overpotential of the Li|30-2DPA-SE|Li cell remains below 60 mV, and it stably cycles for over 1400 hours without any short circuits. In contrast, the overpotential of the PEO/LiTFSI battery starts at 65 mV and approaches 100 mV before a short circuit occurs at 279 hours. The electrode surface in Li|30-2DPA-SE|Li is less deteriorated with fewer dendrites formed after cycling (Fig. S15†). In the long-term cycling, 30-2DPA-SE demonstrates more stable lithium stripping/plating behavior and less deterioration in overpotential, indicating better compatibility with the lithium metal anode, an improvement that stems from the enhanced ion transport, mechanical properties, and interfacial contact (Fig. S16†).

All-solid-state batteries of Li|30-2DPA-SE|LFP and Li|PEO/LiTFSI|LFP were assembled to compare their full battery performance. The battery with 30-2DPA-SE exhibits an initial discharge capacity of 157.4 mA h g^{-1} at 0.2 C (Fig. 4b), which is higher than the 136.4 mA h g^{-1} of the battery with PEO/LiTFSI. In addition, the Li|30-2DPA-SE|LFP battery experiences a capacity increase, reaching a maximum of 165.4 mA h g^{-1} by the 10th cycle. The rise in capacity is due to the decreased impedance before the 10th cycle (Fig. S17†). After 50 cycles, this capacity stabilizes at 149.2 mA h g^{-1} with a coulombic efficiency of 99.6%, still outperforming the Li|PEO/LiTFSI|LFP battery, which has a capacity of 133.1 mA h g^{-1} and a coulombic efficiency of 98.7%. The performance at different charging/discharging rates was also tested (Fig. 4c and d). The Li|30-

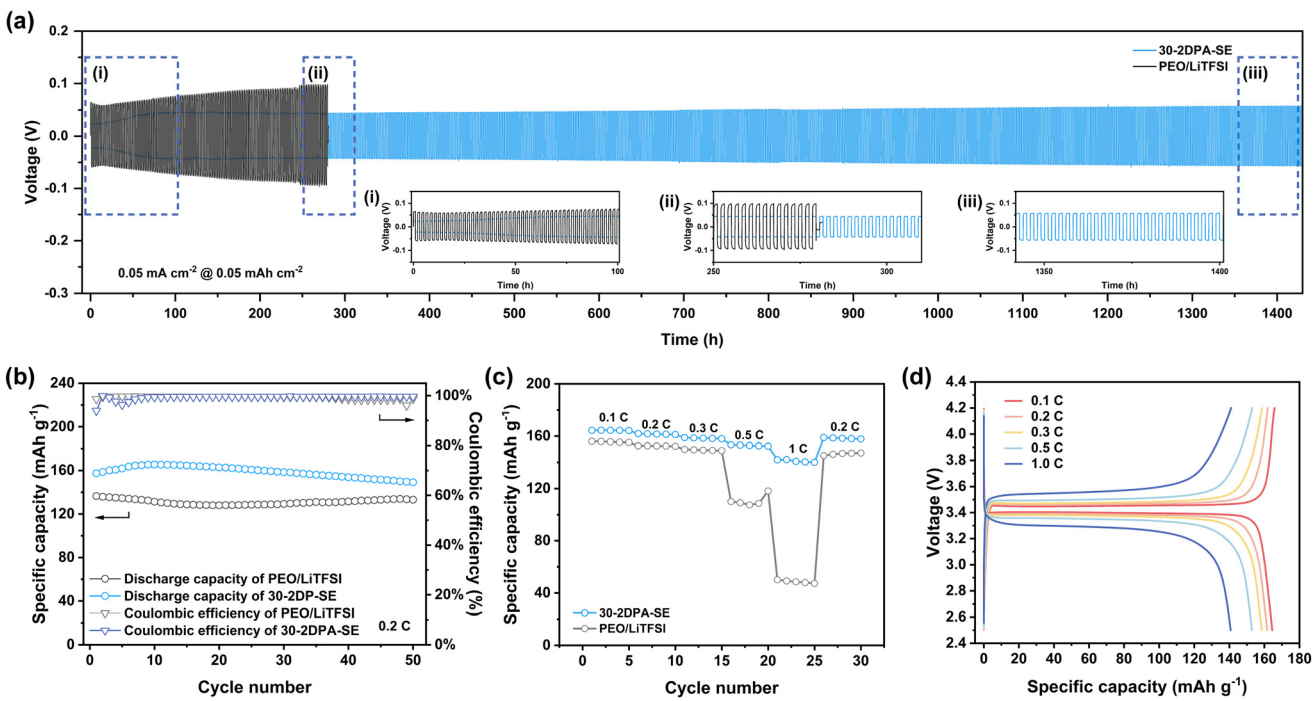

Fig. 4 (a) The long-term cycling performance of lithium stripping/plating at 0.05 mA h cm^{-2} at 50 °C. Insets are the local magnified curves. (b) The cycling performance of Li|SPE|LFP at 0.2 C and 50 °C. (c) The cycling performance of Li|SPE|LFP at different rates at 50 °C. (d) The voltage curves at different charging/discharging rates of Li|30-2DPA-SE|LFP at 50 °C.

2DPA-SE|LFP battery exhibits specific discharge capacities of 158.4, 152.9, and 140.8 mA h g^{-1} at rates of 0.3, 0.5, and 1 C, respectively. In contrast, the Li|PEO/LiTFSI|LFP battery shows lower capacity at varied rates. Furthermore, the Li|30-2DPA-SE|LFP battery exhibits stable charging/discharging voltage platforms from 0.1 to 1 C. When the rate is returned to 0.2 C, the capacity remains similar to the initial value at 0.2 C. This capacity retention indicates good reversibility and minimal irreversible side reactions during charging/discharging at varied rates.

Conclusions

A series of corona-shaped 2DPA-PEG polymers were synthesized and employed as molecular fillers in PEO-based solid polymer electrolytes. The PEG chains on the 2DPA platelets ensure intrinsic compatibility with the PEO matrix through chain entanglements, preventing PEO chain crystallization and enhancing its room-temperature ionic conductivity to 4.39×10^{-5} S cm^{-1}, which is an order of magnitude higher than that of the PEO electrolyte. Meanwhile, the Lewis acid–base interaction between the amides on 2DPA rigid cores and $TFSI^-$ anions debilitates the motion of $TFSI^-$, thereby improving the lithium-ion transference number from 0.12 to 0.78. Furthermore, the electrochemical window is broadened to 4.7 V due to the electron-deficient nature of 2DPA-PEGs. The mechanical properties, including the storage modulus and tan (δ), of the electrolyte are also improved.

The lithium symmetric cell utilizing 30-2DPA-SE showcases superior long-term cycling stability over 1400 hours with a steady overpotential. Moreover, the all-solid-state battery of Li|30-2DPA-SE|LFP delivers a specific discharge capacity of 149.2 mA h g^{-1} after 50 cycles at 0.2 C, maintaining a coulombic efficiency of 99.6%.

In summary, this work provides a heterostructural polymer design strategy that enables better ionic conductivity, higher transference numbers, a broader electrochemical window, and enhanced mechanical properties. We envisage that this design concept may contribute to further research on solid polymer electrolytes.

Author contributions

Feifan Zheng: conceptualization, methodology, investigation, and writing – original draft preparation; Liping Jiang & Xiaoli Gong: investigation and data curation – HR AFM; Zhengqiao Yin: investigation; Fei Wang: validation; and Yuwen Zeng: conceptualization, supervision, funding acquisition, and writing – review & editing.

Data availability

The data supporting this article have been included as part of the ESI.†

Conflicts of interest

There are no conflicts to declare.

Acknowledgements

This work is sponsored by the Shanghai Pujiang Program (22PJ1400500) and the Start-up Fund from Fudan University. The authors also thank Professor Jianan Wang from Xi'an Jiaotong University for his valuable discussions and suggestions.

References

1 B. Acebedo, M. C. Morant-Miñana, E. Gonzalo, I. Ruiz de Larramendi, A. Villaverde, J. Rikarte and L. Fallarino, *Adv. Energy Mater.*, 2023, **13**, 2203744.
2 S. Kim, G. Park, S. J. Lee, S. Seo, K. Ryu, C. H. Kim and J. W. Choi, *Adv. Mater.*, 2023, 2206625.
3 W. Xu, J. Wang, F. Ding, X. Chen, E. Nasybulin, Y. Zhang and J.-G. Zhang, *Energy Environ. Sci.*, 2014, **7**, 513–537.
4 M. Zhang, P. Pan, Z. Cheng, J. Mao, L. Jiang, C. Ni, S. Park, K. Deng, Y. Hu and K. K. Fu, *Nano Lett.*, 2021, **21**, 7070–7078.
5 J. Qian, W. A. Henderson, W. Xu, P. Bhattacharya, M. Engelhard, O. Borodin and J. G. Zhang, *Nat. Commun.*, 2015, **6**, 6362.
6 J. Janek and W. G. Zeier, *Nat. Energy*, 2023, **8**, 230–240.
7 D. Lin, Y. Liu and Y. Cui, *Nat. Nanotechnol.*, 2017, **12**, 194–206.
8 P. Lennartz, B. A. Paren, A. Herzog-Arbeitman, X. C. Chen, J. A. Johnson, M. Winter, Y. Shao-Horn and G. Brunklaus, *Joule*, 2023, **7**, 1471–1495.
9 X. Lu, Y. Wang, X. Xu, B. Yan, T. Wu and L. Lu, *Adv. Energy Mater.*, 2023, 2301746.
10 Y. Zheng, Y. Yao, J. Ou, M. Li, D. Luo, H. Dou, Z. Li, K. Amine, A. Yu and Z. Chen, *Chem. Soc. Rev.*, 2020, **49**, 8790–8839.
11 X. Su, X.-P. Xu, Z.-Q. Ji, J. Wu, F. Ma and L.-Z. Fan, *Electrochem. Energy Rev.*, 2024, **7**, 2.
12 Z. Guo, Y. Wu, X. Li, X. Wu, Q. Hu, Z. Wang, H. Guo, W. Peng, G. Yan and J. Wang, *Ionics*, 2021, **28**, 779–788.
13 H. An, M. Li, Q. Liu, Y. Song, J. Liu, Z. Yu, X. Liu, B. Deng and J. Wang, *Nat. Commun.*, 2024, **15**, 9150.
14 J. Gao, C. Wang, D. W. Han and D. M. Shin, *Chem. Sci.*, 2021, **12**, 13248–13272.
15 H. Zhang, C. Li, M. Piszcz, E. Coya, T. Rojo, L. M. Rodriguez-Martinez, M. Armand and Z. Zhou, *Chem. Soc. Rev.*, 2017, **46**, 797–815.
16 W. Zhang, V. Koverga, S. Liu, J. Zhou, J. Wang, P. Bai, S. Tan, N. K. Dandu, Z. Wang, F. Chen, J. Xia, H. Wan, X. Zhang, H. Yang, B. L. Lucht, A.-M. Li, X.-Q. Yang, E. Hu, S. R. Raghavan, A. T. Ngo and C. Wang, *Nat. Energy*, 2024, **9**, 386–400.

17 G. Homann, L. Stolz, J. Nair, I. C. Laskovic, M. Winter and J. Kasnatscheew, *Sci. Rep.*, 2020, **10**, 4390.
18 Q. Zhao, S. Stalin, C.-Z. Zhao and L. A. Archer, *Nat. Rev. Mater.*, 2020, **5**, 229–252.
19 C. D. Fang, Y. Huang, Y. F. Sun, P. F. Sun, K. Li, S. Y. Yao, M. Y. Zhang, W. H. Fang and J. J. Chen, *Nat. Commun.*, 2024, **15**, 6781.
20 J.-H. Kim, D.-H. Park, J.-S. Jang, J.-H. Shin, M.-C. Kim, S.-B. Kim, S.-H. Moon, S.-N. Lee and K.-W. Park, *Chem. Eng. J.*, 2022, **446**, 137035.
21 P. Zhu, C. Yan, M. Dirican, J. Zhu, J. Zang, R. K. Selvan, C.-C. Chung, H. Jia, Y. Li, Y. Kiyak, N. Wu and X. Zhang, *J. Mater. Chem. A*, 2018, **6**, 4279–4285.
22 Y. Li, L. Zhang, Z. Sun, G. Gao, S. Lu, M. Zhu, Y. Zhang, Z. Jia, C. Xiao, H. Bu, K. Xi and S. Ding, *J. Mater. Chem. A*, 2020, **8**, 9579–9589.
23 X. Yin, L. Wang, Y. Kim, N. Ding, J. Kong, D. Safanama, Y. Zheng, J. Xu, D. V. M. Repaka, K. Hippalgaonkar, S. W. Lee, S. Adams and G. W. Zheng, *Adv. Sci.*, 2020, **7**, 2001303.
24 Q. Pan, Y. Zheng, S. Kota, W. Huang, S. Wang, H. Qi, S. Kim, Y. Tu, M. W. Barsoum and C. Y. Li, *Nanoscale Adv.*, 2019, **1**, 395–402.
25 Y. Li, Y. Qin, J. Zhao, M. Ma, M. Zhang, P. Li, S. Lu, H. Bu, K. Xi, Y. Su and S. Ding, *ACS Appl. Mater. Interfaces*, 2022, **14**, 18360–18372.
26 E. Zhao, Y. Guo, A. Zhang, H. Wang and G. Xu, *Nanoscale*, 2022, **14**, 890–897.
27 V. Bocharova, X. C. Chen, S. P. Jeong, Z. Zhou, R. L. Sacci, J. K. Keum, C. Gainaru, M. A. Rahman, R. Sahori, X.-G. Sun, P. Cao and A. Westover, *ACS Appl. Energy Mater.*, 2023, **6**, 8042–8052.
28 W. Liu, N. Liu, J. Sun, P. C. Hsu, Y. Li, H. W. Lee and Y. Cui, *Nano Lett.*, 2015, **15**, 2740–2745.
29 F. Zheng, C. Li, Z. Li, X. Cao, H. Luo, J. Liang, X. Zhao and J. Kong, *Small*, 2023, **19**, 2206355.
30 Z. Shen, Y. Cheng, S. Sun, X. Ke, L. Liu and Z. Shi, *Carbon Energy*, 2021, **3**, 482–508.
31 Y. Zeng, P. Gordiichuk, T. Ichihara, G. Zhang, E. Sandoz-Rosado, E. D. Wetzel, J. Tresback, J. Yang, D. Kozawa, Z. Yang, M. Kuehne, M. Quien, Z. Yuan, X. Gong, G. He, D. J. Lundberg, P. Liu, A. T. Liu, J. F. Yang, H. J. Kulik and M. S. Strano, *Nature*, 2022, **602**, 91–95.
32 X. Hu, D. Kaplan and P. Cebe, *Macromolecules*, 2006, **39**, 6161–6170.
33 X. Du, Y. Tan, H. Wang, L. Zhang and X. Ren, *J. Polym. Res.*, 2010, **18**, 753–762.
34 X. Tan, Y. Tong, J. Yang, X. Du, A. Yang, A. Zhang and Q. Xu, *Polym. Chem.*, 2024, **15**, 454–464.
35 K. M. Abraham, Z. Jiang and B. Carroll, *Chem. Mater.*, 1997, **9**, 1978–1988.
36 Q. Ma, H. Zhang, C. Zhou, L. Zheng, P. Cheng, J. Nie, W. Feng, Y. S. Hu, H. Li, X. Huang, L. Chen, M. Armand and Z. Zhou, *Angew. Chem., Int. Ed.*, 2016, **55**, 2521–2525.
37 S. Han, P. Wen, H. Wang, Y. Zhou, Y. Gu, L. Zhang, Y. Shao-Horn, X. Lin and M. Chen, *Nat. Mater.*, 2023, **22**, 1515–1522.
38 O. Sheng, C. Jin, J. Luo, H. Yuan, H. Huang, Y. Gan, J. Zhang, Y. Xia, C. Liang, W. Zhang and X. Tao, *Nano Lett.*, 2018, **18**, 3104–3112.
39 Y. F. Zhang, S. L. Bai, D. Y. Yang, Z. Zhang and S. Kao-Walter, *J. Polym. Sci., Part B: Polym. Phys.*, 2007, **46**, 281–288.
40 N. Saba, M. Jawaid, O. Y. Alothman and M. T. Paridah, *Constr. Build. Mater.*, 2016, **106**, 149–159.
41 H. Wu, R. Hu, B. Zeng, L. Yang, T. Chen, W. Zheng, X. Liu, W. Luo and L. Dai, *RSC Adv.*, 2018, **8**, 37631–37642.
42 S. Lu, S. Chen, L. Luo, Y. Yang, J. Wang, Y. Chen, Y. Yang, Z. Yuan and X. Chen, *ACS Chem. Health Saf.*, 2023, **30**, 343–361.
43 A. Casu, G. Camino, M. De Giorgi, D. Flath, V. Morone and R. Zenoni, *Polym. Degrad. Stab.*, 1997, **58**, 297–302.